UC Davis
Civil & Environmental Engineering

Title

Effect of Anisotropic Consolidation on Cyclic Liquefaction Resistance of Granular Materials via 3D-DEM Modeling

Permalink

https://escholarship.org/uc/item/5rv3d8np

Journal

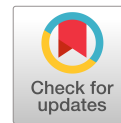Journal of Geotechnical and Geoenvironmental Engineering, 150(5)

Authors

Yang, Ming

Taiebat, Mahdi

Publication Date

2024-05-01

Peer reviewed

Effect of Anisotropic Consolidation on Cyclic Liquefaction Resistance of Granular Materials via 3D-DEM Modeling

Ming Yang[1] and Mahdi Taiebat, M.ASCE[2]

Abstract: The influence of anisotropic consolidation on the cyclic liquefaction resistance of granular materials is explored using 3D discrete element method simulations. In this study, the term anisotropic consolidation was defined as the ratio of initial horizontal and vertical normal stresses, and the hypothesis was that the conflicting results from previous laboratory experiments could be attributed to differences in inherent fabric. To test this hypothesis, three unique sample preparation protocols were employed to construct polydisperse spherical particle samples with varying inherent fabrics, as quantified by coordination number and contact-normal fabric anisotropy, under consistent initial mean stress and density conditions. The results were intriguing, as they revealed that anisotropic consolidation had a consistent impact on the cyclic liquefaction resistance of loose and medium-dense samples, regardless of preparation protocol. However, this relationship was not as straight-forward in dense samples. In addition, the study assessed the correlations between various parameters, including initial shear wave velocity, state parameters associated with both void ratio and coordination number, fabric anisotropy, and their impact on the cyclic liquefaction resistance of the samples. The findings enhance the understanding of the intricate interplay between anisotropic consolidation and the resistance of granular materials to cyclic liquefaction, providing valuable insights that can inform the development of accurate models for predicting and mitigating cyclic liquefaction in various applications. **DOI: 10.1061/JGGEFK.GTENG-11970.** © 2024 American Society of Civil Engineers.

Introduction

Nonlinear deformation analysis for seismic site response involving sand liquefaction via a continuum mechanics-based numerical modeling approach requires representative constitutive models. Such models must incorporate essential constitutive ingredients that play key roles in capturing the dominant aspects of response under the cyclic shearing of sands. Laboratory element-level tests on samples with different initial and cyclic shearing conditions are the primary source of information for decoding the mechanism and translating those to constitutive ingredients in the stress–strain models. Over the last four decades, laboratory element-level tests on cyclic shearing of sands have investigated the effect of particle-level properties such as particle size distribution and particle shape, and sample homogenized properties such as density, confining pressure, inherent anisotropy, and anisotropic consolidation, among others.

Among the many laboratory experiments on cyclic liquefaction, a small fraction has focused on deciphering the role of anisotropic consolidation on the undrained cyclic response of sands. Anisotropic consolidation is quantified by the initial consolidation stress ratio K_c, defined as the ratio of the initial horizontal and vertical normal stresses, namely $K_c = \sigma_{h0}/\sigma_{v0}$. For samples prepared with all shear stress components zero, $K_c = 1$ corresponds to an isotropic stress state, and $K_c \neq 1$ refers to an anisotropic stress state. These samples are then subjected to undrained cyclic simple shearing, often under constant shear stress amplitude τ^{amp}, until initial liquefaction to determine the corresponding cyclic liquefaction resistance. Ishihara et al. (1977) and Ishihara and Takatsu (1979) studied the effect of K_c values, including 0.5, 1.0, and 1.5, on the cyclic liquefaction resistance of fine Fuji river sand at relative density $D_r = 55\%$ and $\sigma_{v0} = 100$ kPa. With cyclic stress ratio (CSR) defined by the ratio of the shear stress amplitude and the initial vertical effective stress, i.e., $CSR = \tau^{amp}/\sigma_{v0}$, they observed that the cyclic liquefaction resistance increases with increasing K_c. Ishihara et al. (1977) proposed a formula linking the cyclic resistance ratio (CRR), namely CSR, required to induce initial liquefaction in the specified number of loading cycles, of anisotropically consolidated (AC) samples with that of isotropically consolidated (IC) samples

$$\mathrm{CRR_{AC}} = \frac{1 + 2K_c}{3} \mathrm{CRR_{IC}} \qquad (1)$$

which applied well to their experimental data. Tatsuoka et al. (1982) performed similar laboratory experiments on Toyoura sand at a wide range of D_r from 35% to 80% under an initial mean effective stress $p_0 = 98$ kPa and with two K_c values of 0.5 and 1. They defined a different $CSR = \tau^{amp}/p_0$, and noticed that the cyclic liquefaction resistance of AC specimens was similar to those of IC specimens for $D_r < 65\%$ and much larger than those of IC specimens for $D_r > 70\%$. Their observation about samples with $D_r < 65\%$ is consistent with that of Ishihara et al. (1977) since the above formula becomes

$$\mathrm{CRR_{AC}} = \mathrm{CRR_{IC}} \qquad (2)$$

with the adoption of $CSR = \tau^{amp}/p_0$ instead of τ^{amp}/σ_{v0}. Meanwhile, the observation of Tatsuoka et al. (1982) about samples with $D_r > 70\%$ questions the general validity of Eqs. (1) or (2). Boulanger and Seed (1995) studied modified Sacramento River sand samples consolidated at $\sigma_{v0} = 207$ kPa to reach D_r values of 35% and 55%, covering three different K_c values of 0.3, 0.5, and 1. Using $CSR = \tau/\sigma_{v0}$, it was found that K_c values of 0.3 and 0.5 resulted in similar cyclic liquefaction resistance, while the IC sample showed about 10% greater liquefaction resistance. This implies that AC samples have higher liquefaction resistance than IC samples

[1]Postdoctoral Scholar, Dept. of Civil and Environmental Engineering, Northwestern Univ., Evanston, IL 60201. ORCID: https://orcid.org/0000-0002-6409-3942. Email: myang@northwestern.edu

[2]Professor, Dept. of Civil Engineering, Univ. of British Columbia, Vancouver, BC, Canada V6T 1Z4 (corresponding author). ORCID: https://orcid.org/0000-0003-2067-8161. Email: mtaiebat@civil.ubc.ca

© ASCE 04024028-1 J. Geotech. Geoenviron. Eng.

J. Geotech. Geoenviron. Eng., 2024, 150(5): 04024028

for $D_r = 35\%$ and 55% with the adoption of $\mathrm{CSR} = \tau^{\mathrm{amp}}/p_0$. Hosono and Yoshimine (2008) considered Toyoura sand at $D_r \simeq 40\%$ with a wide range of K_c values from 0.25 to 4, but these different K_c samples do not share the same p_0 or σ_{v0}. By adopting $\mathrm{CSR} = \tau^{\mathrm{amp}}/\sigma_{v0}$, they concluded that the cyclic liquefaction resistance increased with increasing K_c. By correcting CSR with respect to p_0 and neglecting the effect of differences in p_0, there does not exist a monotonic relationship between liquefaction resistance and K_c, but it is clear that the AC sample with $K_c = 0.5$ presents higher liquefaction resistance than the IC sample. Georgiannou and Konstadinou (2014) applied a different type of undrained cyclic torsional loading on Ottawa sand consolidated at $p_0 = 110$ kPa and with various D_r from 20% to 65%, considering two K_c values of 0.5 and 1, and unlike others, the total boundary normal stresses were held constant instead of constraining normal strains in the conventional undrained simple shear test. They pointed out that the AC sample at a loose state is less than half the cyclic liquefaction resistance of the IC sample, and this trend reversed at the dense state ($D_r > 60\%$), implying the existence of a density where AC and IC samples share similar liquefaction resistance. Recently, Vargas et al. (2020) performed conventional undrained cyclic torsional tests on Ottawa-F65 sand under $p_0 = 100$ kPa and at D_r values of 50% and 70%, covering two K_c values of 0.5 and 1. With the same CSR definition as Tatsuoka et al. (1982), they observed that the liquefaction resistance of AC samples is approximately 20% higher than that of IC samples at both D_r values.

Despite efforts to use a consistent definition of CSR in interpreting the laboratory experiments introduced above, a universal or even consistent answer to the effect of K_c on the cyclic liquefaction resistance of granular materials remains elusive. This is due in part to the inconsistencies across laboratory experiments in particle properties, sample reconstitution methods, specimen densities and confinements, and cyclic loading programs, which can result in variations in the experimental results. Although the effects of these factors are discernible, their independent contributions to the effect of K_c on liquefaction characteristics of granular materials have not been precisely identified. For instance, while most of the relevant laboratory experiments have focused on medium-dense and dense sands, the effect of K_c on loose sand response cannot be extrapolated from the dense cases. Furthermore, as most previous studies involve samples consolidated at a confinement of nearly 100 kPa, it is uncertain whether these observations can be extended to samples with higher or lower consolidation stress. It is also unclear whether the knowledge gained about K_c effect on reconstituted samples following air pluviation can be applied to the samples prepared via wet sedimentation. In addition, elucidating the underlying mechanism that explains the macroscopic response is a challenge for laboratory experiments that only measure stresses and strains at the sample scale and do not provide access to particle-level screening.

While laboratory experiments are valuable for enriching the database of the K_c effect on cyclic liquefaction resistance, the discrete element method (DEM) offers an alternative numerical approach. This method enables the study of granular systems and provides the additional benefit of assessing the micromechanics of the system, making it a promising tool to investigate the relationship between microscopic fabric and macroscopic response. The particle dynamic DEM has been widely utilized to simulate the cyclic liquefaction response of granular materials, unveiling the microscopic signature of the jamming transition (e.g., Sitharam 2003; Wang and Wei 2016; Huang et al. 2018; Wei et al. 2018; Zhang and Evans 2020; Xu et al. 2021; Yang et al. 2021, 2022a). Recently, Rahman et al. (2021) highlighted the application of the critical state soil mechanics (CSSM) framework for cyclic liquefaction assessment, which was proposed by Jefferies and Been (2015), in linking CRR of cyclic

triaxial simulations with the initial state parameter ψ_{e0} of the sample at presshearing. Gu et al. (2020) raised a concern regarding the relationship between the CRR and the ψ_{e0} since one can prepare another sample at the same density but with different coordination numbers, whose CRR will be noticeably different from that of the original sample. They proposed linking CRR to ψ_{z0}, the initial state parameter associated with coordination number z, instead. Banerjee et al. (2023) found good correlations between either one of the initial state parameters and the CRR in samples with different particle size distributions. In addition, Wei and Wang (2017) prepared DEM samples with the same density, but with different fabric anisotropies that were quantified by both coordination number and contact-normal fabric anisotropy, where the sample with higher fabric anisotropy had a lower coordination number. It was also revealed that the resistance to cyclic liquefaction decreased as fabric anisotropy increased, or coordination number decreased. Otsubo et al. (2022) successfully isolated fabric anisotropy from other lower-order descriptors by constructing DEM samples at the same void ratio, stress conditions, and coordination number but different fabric anisotropies. They observed that samples with a high degree of anisotropy tend to deform more in their weaker direction at an early stage of undrained cyclic loading, leading to lower liquefaction resistance than samples with isotropic fabric.

In this study, DEM is used to investigate the impact of anisotropic consolidation on the cyclic liquefaction response of granular materials. Samples of spherical particles were first created using a typical DEM sample preparation protocol at loose, medium-dense, and dense states with a mean pressure of 100 kPa and K_c values of 0.5 and 1. To further understand how the *inherent fabric* and K_c values affect the cyclic liquefaction resistance of granular materials, two new sample preparation protocols were introduced to reduce the high contact density in the dense samples while maintaining the void ratio. It must be noted that the current study does not separate the coordination number from fabric anisotropy in measuring inherent fabric. This limitation can be the subject of future works. Constant-volume cyclic shearing was performed on these samples to determine their cyclic liquefaction resistance. It was found that the effect of K_c on the cyclic liquefaction resistance of dense samples depends on the sample preparation protocol. The observed K_c effects on cyclic liquefaction resistance were attributed to the initial properties of the samples before shearing and good correlations between liquefaction resistance and indicators related to the inherent fabric were observed in most of the numerical experiments.

DEM Setup

The open-source DEM program LIGGGHTS (Kloss et al. 2012) was used to simulate particle dynamics in the study. The granular assembly consisted of polydisperse spherical particles that interacted through soft-contact laws. These laws comprised a Hertzian normal model and a history-dependent tangential model with a Coulomb friction cut off. The modified elastic-plastic spring dashpot model EPSD3 (Ai et al. 2011) was adopted to incorporate rolling resistance into spherical particles, which provided a simple way to account for the effects of aspherical particle shape or surface roughness (Radja and Dubois 2011). Details of the contact models are available in the LIGGGHTS documentation.

The corresponding DEM parameters, including particle density ρ, particle Young's modulus E, Poisson's ratio ν, coefficient of restitution ε, tangential friction coefficient μ, rolling friction coefficient μ_r, rolling viscous damping coefficient η_r, and rolling stiffness coefficient β, are listed in Table 1. The values of E and ν were borrowed from Sufian et al. (2017) to simulate nearly undeformable

Table 1. DEM parameters

Description	Value
Particle density, ρ(kg/m^3)	2,650
Young's modulus, E(GPa)	70
Poisson's ratio, ν	0.25
Coefficient of restitution, ε	0.8
Tangential friction coefficient, μ	0.5
Rolling friction coefficient, μ_r	0.1
Rolling viscous damping coefficient, η_r	0.13
Rolling stiffness coefficient, β	2.25

particles, which required a high E value so that the average normal deflection between particles was negligible compared with the particle size. A high value of ε was chosen to introduce a low viscous force for "weak" dissipation of kinetic energy of colliding particles. A value of $\mu = 0.5$ was commonly used in the literature for the shearing stage (e.g., Guo and Zhao 2013; Rahman et al. 2021) to ensure the DEM sample presented a reasonable critical state friction angle. The value of μ_r was set to a small nonzero number to enhance dissipation while sliding friction remained the main effect. The other rolling parameters were set to default values suggested in the LIGGGHTS documentation. LIGGGHTS adopts an explicit velocity-Verlet time-stepping scheme to update positions, and linear and angular velocities of spherical particles. A time step size $\Delta t = 2 \times 10^{-9}$ s was determined to be less than 5% of the Rayleigh (wave propagation time scale) and Hertz (contact time scale) time step sizes, ensuring enough accuracy of numerical simulations.

The simulations involved two main phases: (1) constructing DEM samples via isotropic/anisotropic compression, and (2) applying cyclic simple shearing to the sample under constant-volume conditions.

Sample Preparation

All DEM samples in the study consisted of 15,625 spherical particles, divided into ten discrete subclasses with distinct particle sizes. The number of particles in each subclass was calculated according to the approach presented in Mutabaruka et al. (2019), such that the particle size distribution nearly followed that of Ottawa-F65 sand (Ghoraiby et al. 2020), while neglecting very small and large particles with inappreciable volume fractions. Fig. 1(a) presents the target and resulting particle size distributions. It should be noted that this study only utilizes Ottawa-F65 sand as a reference to construct

the DEM sample, without the aim of precisely replicating the sand's characteristics. The quantitative validation of the DEM model and the laboratory experiments on Ottawa-F65 sand is not pursued within the scope of this study.

The particles were randomly generated and placed on a three-dimensional (3D) sparse lattice of $25 \times 25 \times 25$ to avoid overlap. This 3D lattice was contained in a rectangular cell with all six sides being rigid walls. The sample was then constructed by translating the six sides of the cell to achieve the final target mean pressure p_0, following the four stages of sample preparation outlined in Yang et al. (2021): (1) using a small μ_I, densifying the sparse cell by moving the six rigid walls at a constant small velocity until the void ratio e reached 1.2, (2) setting the velocities of the six rigid walls to zero and using a servo-control algorithm to compress the sample isotropically to the target mean pressure $p = 0.1 p_0$ with the same μ_I, (3) replacing the four lateral walls with periodic boundaries, increasing the target mean pressure to $0.2 p_0$, and continuing isotropic compression of the sample with the same μ_I, and (4) modifying μ to 0.5 to further compress the sample isotropically or anisotropically to the final target mean pressure $p = p_0$. Fig. 1(b) provides a snapshot of a sample that was prepared using this protocol.

The anisotropic compression in stage 4 was realized by setting different target vertical and horizontal normal stresses to the top and bottom rigid walls and four lateral periodic boundaries, respectively. More specifically, with the given consolidation stress ratio K_c, the target vertical normal stress (σ_{zz}) was $\sigma_{v0} = 3 p_0/(1 + 2K_c)$ and the target horizontal normal stress (σ_{xx} and σ_{yy}) was $\sigma_{h0} = K_c \sigma_{v0}$. The aforementioned four-stage sample preparation protocol was denoted as protocol A (PA). Fig. 2 presents the schematic stress paths, including the last three stages of PA, given the zero-stress state in stage 1. It should be noted that the simulated stress path between σ_v and σ_h in each stage may not follow the linear trend of Fig. 2, which heavily depends on the servo-control algorithm. The first six rows in Table 2 list the samples prepared by following PA, including anisotropically consolidated (AC) and isotropically consolidated (IC) dense (D), medium-dense (M), and loose (L) samples.

One of the signatures of the dense samples prepared using the protocol PA is that they show noticeably high contact density (number of contacts per unit volume). This is a direct result of the use of small tangential friction μ_I in the first three stages of preparing the PA dense samples, which is analogous to partially lubricating contacts in the assembling stage. To mitigate this issue, protocol B (PB) was introduced, which involved subjecting the samples of PA to a
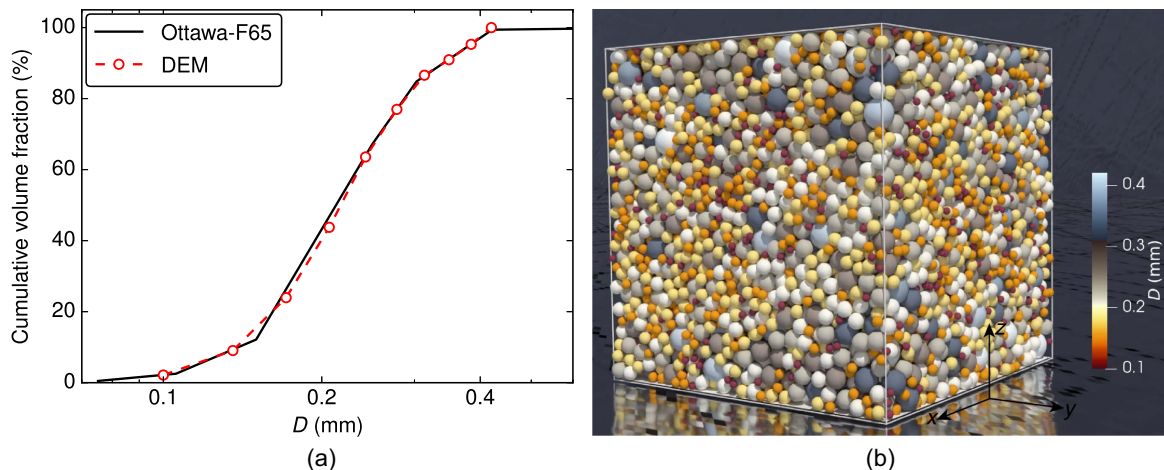

Fig. 1. (a) Particle size distributions; and (b) snapshot of the simulated sample composed of 15,625 particles.
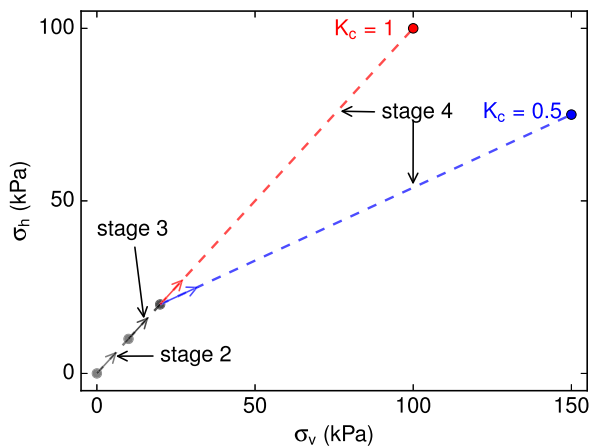
Fig. 2. Stress paths for preparing anisotropic samples with varying initial consolidation ratio K_c, showing stages 2–4 of the sample preparation process.

Table 2. Properties of DEM samples at $p_0 = 100$ kPa ($e_{max} \simeq 0.669$, $e_{min} \simeq 0.510$)

Sample ID	μ_I	K_c	e_0	D_r (%)	G_0 (MPa)	z_{m0}	a_{c0}	e_c	z_{mc}
PA-AC-D	0.1	0.5	0.586	52.2	105.8	5.45	0.06	0.654	4.44
PA-IC-D	0.1	1.0	0.586	52.2	129.7	5.61	0.05	0.665	4.44
PA-AC-M	0.2	0.5	0.620	30.8	50.6	4.67	0.17	0.677	4.26
PA-IC-M	0.2	1.0	0.620	30.8	84.1	4.94	0.04	0.684	4.28
PA-AC-L	0.4	0.5	0.653	10.1	22.1	4.33	0.37	0.687	4.23
PA-IC-L	0.4	1.0	0.659	6.3	34.9	4.44	0.08	0.692	4.26
PB-AC-D	0.1	0.5	0.585	52.8	50.1	4.66	0.18	0.664	4.27
PB-IC-D	0.1	1.0	0.585	52.8	55.0	4.71	0.15	0.665	4.24
PB-AC-M	0.2	0.5	0.614	34.6	33.2	4.39	0.26	0.676	4.21
PB-IC-M	0.2	1.0	0.615	33.9	36.5	4.44	0.16	0.674	4.19
PB-AC-L	0.4	0.5	0.630	24.5	25.6	4.29	0.34	0.684	4.14
PB-IC-L	0.4	1.0	0.638	19.5	28.0	4.31	0.19	0.682	4.16
PC-AC-D1	0.2	0.5	0.583	54.1	66.9	5.00	0.17	0.661	4.36
PC-IC-D1	0.2	1.0	0.583	54.1	87.9	5.15	0.04	0.660	4.38
PC-AC-D2	0.3	0.5	0.586	52.2	46.7	4.68	0.27	0.667	4.28
PC-IC-D2	0.3	1.0	0.586	52.2	63.4	4.85	0.06	0.663	4.30
PC-AC-D3	0.4	0.5	0.589	50.3	38.1	4.59	0.28	0.661	4.29
PC-IC-D3	0.4	1.0	0.589	50.3	49.4	4.69	0.01	0.661	4.30
PC-AC-M1	0.3	0.5	0.622	29.6	34.7	4.55	0.24	0.684	4.27
PC-IC-M1	0.3	1.0	0.622	29.6	57.5	4.75	0.03	0.681	4.28
PC-AC-M2	0.4	0.5	0.623	28.9	29.6	4.45	0.29	0.679	4.25
PC-IC-M2	0.4	1.0	0.623	28.9	43.9	4.57	0.03	0.681	4.25
PC-AC-L	0.45	0.5	0.648	13.2	21.3	4.34	0.34	0.688	4.23
PC-IC-L	0.45	1.0	0.650	11.9	31.7	4.40	0.06	0.691	4.22

fifth stage to reduce the contact density while aiming to maintain the same sample density. Adopting the approach introduced by (Agnolin and Roux 2007), this fifth stage of PB involved applying a homogeneous expansion, where all coordinates were multiplied by a common factor λ slightly greater than 1. Velocities were assigned to particles in all three spatial directions, where each component was chosen randomly from a range between $-v_I$ and v_I, and the servo-control algorithm was continued with $\mu = 0.5$ to reach the target stress state. Six DEM samples were prepared via PB with $\lambda = 1.0005$ and $v_I = 0.02$ m/s as presented in Table 2, where, for example, PB-AC-D refers to the sample PA-AC-D that was subjected to the fifth stage of sample preparation as explained above.

In addition to PB, another alternative referred to as protocol C (PC) was also introduced to mitigate the issue of high contact

density in PA because of the use of small μ_I. Inspired by the work of Kuhn et al. (2014), the PC followed the same four stages of PA, with the only difference being in stage (2): during the servo-control isotropic compression in this stage, velocities were assigned to particles in all three spatial directions at every certain number of analysis steps denoted as n_{stage}. Each velocity component was chosen randomly from a range between $-v_I$ and v_I. The choices of μ_I, v_I, and n_{stage} will determine the stable packing density of the DEM sample, requiring iterative trials to prepare PC samples with similar densities to the PA samples. The last few rows in Table 2 present the prepared PC samples, where $v_I = 0.13$, 0.07, and 0.03 m/s are used to construct dense, medium-dense, and loose samples, respectively, with $n_{stage} = 10^5$. Unlike the single pair of PA or PB dense samples, consisting of samples with the same density and pressure but different K_c values (i.e., the IC and AC samples), three pairs of PC dense samples were included due to variations in μ_I. This decision was made because these PC dense samples exhibited distinct responses to anisotropic consolidation. Additional pairs of PA or PB dense samples were generated by introducing controlled disturbances, such as varying particle initial positions in the PA samples or using different λ values in the PB samples. However, these disturbances did not result in discernible differences in relative liquefaction resistance. Furthermore, in Table 2, two pairs of PC medium-dense samples were included to emphasize that the observed distinctions in PC dense samples do not necessarily extend to PC medium-dense (and even loose) samples, as will be illustrated in the next section.

Simple Shearing

The cyclic simple shearing simulation was carried out using a numerical model with biperiodic lateral side boundaries. To maintain a constant sample volume, four lateral sides and the bottom wall were fixed, while the sample height h was kept constant. The top wall was moved horizontally along the x axis at a constant velocity v_x to impose the cyclic shearing. To prevent slippage between the walls and the sample, a layer of particles was glued to the top and bottom walls, respectively. The kinematics of these particles only followed the imposed velocity on the walls. The direction of shear was reversed each time the magnitude of shear stress τ, obtained from the calculated stress tensor, reached a target amplitude τ^{amp}. Unless explicitly stated otherwise, by default, this study adopts the CSR defined by the ratio

$$CSR = \frac{\tau^{amp}}{p_0} \qquad (3)$$

namely normalizing τ^{amp} by the initial mean stress p_0. The biperiodic boundary conditions ensured that the lateral sides of the sample were replicated periodically, so that the sample appeared infinite in the lateral directions. This is in contrast to the Cambridge- or NGI-type simple shear devices, where the lateral sides of the sample are rotated by horizontal movement of the top wall.

The appropriate shear rate was determined by evaluating the inertial number $I = \dot{\gamma}\,\overline{d}\,\sqrt{\rho/p}$, where $\dot{\gamma} = |v_x|/h$ denotes the shear rate, h is the sample height, and ρ and $\overline{d}$ represent the solid density and mean particle diameter, respectively. The inertial number represents the shear rate normalized by the relaxation rate under the action of the average pressure p. The shearing is practically quasistatic if $I < 10^{-3}$ (MiDi 2004). When the sample liquefies, the average pressure, p, degrades to vanishingly small values due to unjamming, which may cause the inertial number, I, to increase beyond 10^{-3} regardless of its value before liquefaction. In the studied experiment, the shear rate, $\dot{\gamma}$, was set to 1 s^{-1} to increase simulation speed while maintaining quasistatic shearing during jammed states. The higher

© ASCE 04024028-4 J. Geotech. Geoenviron. Eng.

J. Geotech. Geoenviron. Eng., 2024, 150(5): 04024028

values of I at unjamming occur as a result of unstable deformation and sudden decrease of p, which is an intrinsic feature of cyclic liquefaction only and not influenced by the loading rate.

Initial Fabric Description

Two micromechanical contact-based indicators, namely the mechanical coordination number z_m and fabric anisotropy a_c, were adopted in this study to quantify the *inherent fabric* of DEM samples. The mechanical coordination number z_m is defined as the average number of contacts per particle, excluding particles with zero and one contact as these particles do not contribute to expanding force network (Thornton 2000)

$$z_m = \frac{2N_c - N_p^1}{N_p - N_p^0 - N_p^1} \tag{4}$$

where N_c = number of contacts; N_p = number of particles; and N_p^0 and N_p^1 are the numbers of particles with zero and one contact, respectively. The fabric anisotropy a_c represents the deviatoric invariant of the fabric anisotropy tensor $\boldsymbol{a}_c$, quantifying the degree of geometrical anisotropy related to the directional distribution of contact normals $\boldsymbol{n}$ (Kanatani 1984)

$$a_c = \sqrt{\frac{3}{2}\boldsymbol{a}_c : \boldsymbol{a}_c} \tag{5a}$$

$$\boldsymbol{a}_c = \frac{15}{2}\left(\boldsymbol{\phi}_c - \frac{1}{3}\boldsymbol{I}\right) \tag{5b}$$

$$\boldsymbol{\phi}_c = \frac{1}{N_c}\sum_{c \in N_c} \boldsymbol{n} \otimes \boldsymbol{n} \tag{5c}$$

Here, $\boldsymbol{I}$ = second-order identity tensor; $\boldsymbol{\phi}_c$ = fabric tensor related to $\boldsymbol{n}$ (Oda 1982); and $\otimes$ = tensor dyadic product.

The initial values of z_m and a_c for samples prior to shearing are provided in Table 2, and their variations with D_r are presented in Fig. 3. It is observed that z_{m0} increases with increasing D_r for all samples, with IC samples always presenting higher z_{m0} and lower a_{c0} than their AC counterparts. At similar D_r, PA samples generally exhibit higher z_{m0} and lower a_{c0} compared with PB and PC ones, confirming the aforementioned that PA specimens tend to have larger contact densities. For PA and PB samples, the gap in a_{c0} between AC and IC specimens reduces with increasing D_r, but this does not apply to PC samples. Different from IC samples of PA and PC with small a_{c0}, PB-IC ones show noticeably higher a_{c0} values.
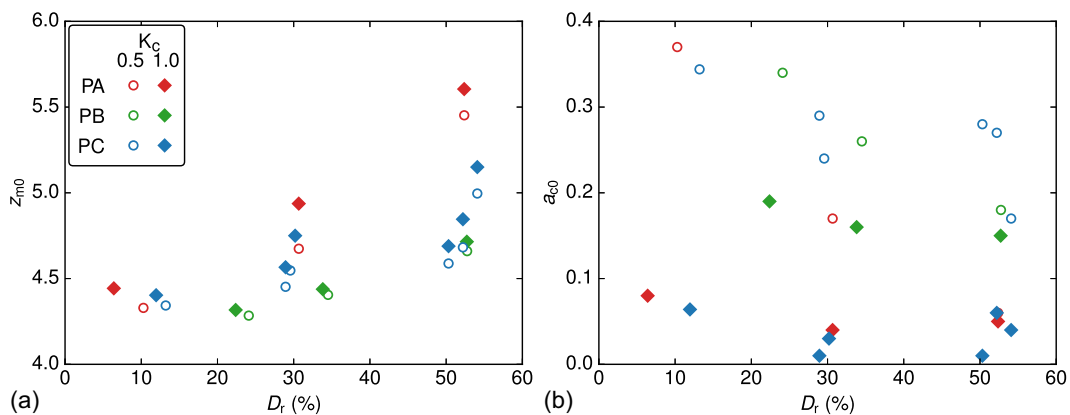
These packing properties will be linked to the cyclic liquefaction response of the samples, as revealed later.

Macroscopic Response

The stress tensor $\boldsymbol{\sigma}$ of the granular packing was obtained by volumetrically averaging the particle stress tensor $\boldsymbol{\sigma}^p$ for particles in the selected region $\mathcal{B}$ (e.g., O'Sullivan 2011; Kuhn 2017)

$$\boldsymbol{\sigma} = \frac{1}{V^{\mathcal{B}}}\sum_{p \in \mathcal{B}} V^{p,\mathcal{B}} \boldsymbol{\sigma}^p \tag{6}$$

where $V^{\mathcal{B}}$ = volume of the region $\mathcal{B}$; and $V^{p,\mathcal{B}}$ = intersection volume of particle p and region $\mathcal{B}$. If particle p is completely contained in the region $\mathcal{B}$, $V^{p,\mathcal{B}}$ is equal to the particle's volume, V^p. The particle stress tensor $\boldsymbol{\sigma}^p$ was determined with respect to the contact forces against neighboring particles or boundaries and the distances between the particle center and contact point as follows:

$$\boldsymbol{\sigma}^p = \frac{1}{V^p}\sum_{c \in \mathcal{C}^p} \boldsymbol{r}^{c,p} \otimes \boldsymbol{f}^{c,p} \tag{7}$$

where $\mathcal{C}^p$ = contact set of particle p; $\boldsymbol{r}^{c,p} = \boldsymbol{r}^c - \boldsymbol{r}^p$ connects the contact point c and the center of particle p; and $\boldsymbol{f}^{c,p}$ = contact force exerted on particle p at the contact point c. In the simple shear test, the shear stress τ and mean effective stress p were calculated as $\tau = \sigma_{zx}$ and $p = (\sigma_{xx} + \sigma_{yy} + \sigma_{zz})/3$, respectively.

The DEM simulations did not explicitly simulate pore water; however, the deduced excess pore pressure in the equivalent undrained system with an incompressible fluid was computed as the variation of the simulated reduction in mean effective stress, i.e., $\Delta u = p_0 - p$. The excess pore pressure ratio was given by $r_u = \Delta u/p_0 = 1 - p/p_0$. The shear strain γ was defined as the ratio x_w/h, where x_w represents the cumulative horizontal displacement of the top wall. The number of cycles N was used as a time variable instead of the running time t, where a fractional number was defined by interpolation between two successive cycles. Specifically, a cycle started with $\gamma = 0$, reached a quarter when γ attained the positive amplitude, became a half when γ dropped back to zero, and approached the third quarter with the negative amplitude of γ.

Results from PA Samples

Fig. 4 displays the simulated macroscopic response of PA dense samples subjected to constant-volume cyclic simple shearing of
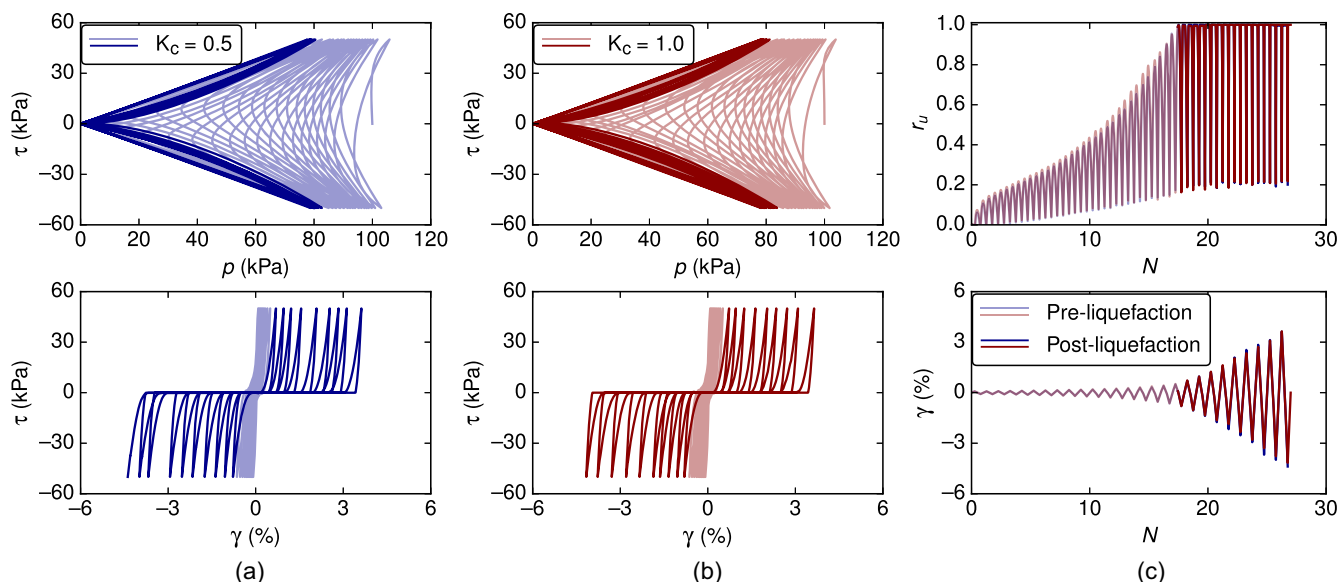

Fig. 3. Variations of (a) initial mechanical coordination number z_{m0}; and (b) initial contact normal-based fabric anisotropic a_{c0}, of the DEM samples with their D_r.

© ASCE   04024028-5   J. Geotech. Geoenviron. Eng.

J. Geotech. Geoenviron. Eng., 2024, 150(5): 04024028

Fig. 4. Macroscopic response of constant-volume cyclic simple shear simulations for PA dense samples under CSR = 0.50: (a) data for $K_c = 0.5$ (PA-AC-D); (b) data for $K_c = 1.0$ (PA-IC-D); and (c) comparing the samples for evolutions of excess pore pressure ratio and shear strain.

magnitude CSR = 0.50. The figure includes the stress paths of shear stress τ versus mean effective stress p, the stress–strain loops of shear stress τ versus shear strain γ, the evolution of excess pore pressure ratio r_u, and the development of shear strain γ. The simulations presented in Figs. 4(a and b) correspond to the anisotropically consolidated sample with $K_c = 0.5$ (PA-AC-D), and isotropically consolidated sample with $K_c = 1.0$ (PA-IC-D), respectively.

The simulations start from $p = 100$ kPa, $\tau = 0$ kPa, and $\gamma = 0$. As τ oscillates in the range of $\pm\tau^{amp}$, p declines gradually, which translates to the evolution of the deduced r_u. The reverse loading after each dilative phase (p increasing) shows an accelerated pace of increase of r_u, while shear strain develops mildly at the same time. The first time that p drops below 1 kPa or r_u reaches above 0.99 is named *initial liquefaction* and the corresponding number of cycles is denoted as N_{IL}, describing cyclic liquefaction resistance. The cyclic shearing stages before and after initial liquefaction are referred to as pre- and post-liquefaction periods, respectively, which are distinct in light and dark colors in Fig. 4. The post-liquefaction stress path gets trapped in a typical *butterfly* shape, and the corresponding stress-strain loops keep expanding at each cycle—a manifestation of the so-called *cyclic mobility*.

Fig. 4 reveals similar macroscopic responses for both PA-AC-D and PA-IC-D samples. However, a detailed inspection of the responses reveals that all three normal stress components of PA-AC-D do not exhibit the same decreasing rate because they vanish at the same time at initial liquefaction. This indicates that the vertical normal stress presents a higher decreasing rate than the horizontal normal ones (Vargas et al. 2020). Additionally, the variations of lateral stress ratio K_h for AC and IC samples are different, as depicted in Fig. 5, where $K_{hx} = \sigma_{xx}/\sigma_{zz}$ and $K_{hy} = \sigma_{yy}/\sigma_{zz}$. The K_h of the IC sample stays around 1, whereas the K_h of the AC sample increases gradually from the initial value of 0.5 to 1, which is consistent with the observations of Ishihara et al. (1977).

The macroscopic response of PA medium-dense samples under CSR = 0.20 and PA loose samples under CSR = 0.08 were simulated, and the results are presented in Figs. 6 and 7, respectively. Each figure includes both anisotropically and isotropically compressed samples. The overall response in Fig. 6 is similar to the response in Fig. 4. However, the anisotropically compressed sample
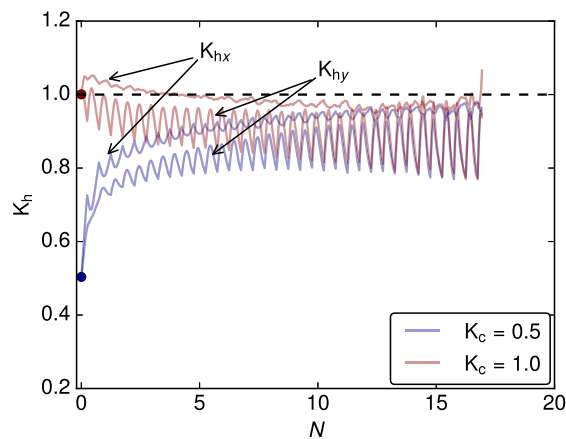

Fig. 5. Variations of horizontal stress ratio $K_h = \sigma_h/\sigma_v$ in the pre-liquefaction stage during cyclic simple shearing for PA dense samples under CSR = 0.50.

PA-AC-M liquefies in a lower number of cycles than the isotropically compressed sample PA-IC-M.

For the loose samples shown in Fig. 7, the stress path results indicate that after a certain number of loading cycles, the samples cannot provide enough shear strength to reach the specified τ^{amp}. This is highlighted by the star marker and is referred to as *cyclic instability*, followed by *flow liquefaction*. This phenomenon is widely observed in loose saturated granular materials subjected to cyclic shearing. Different from the dense case and similar to the medium-dense sample, the number of loading cycles for PA-AC-L sample to reach initial liquefaction is apparently smaller than for PA-IC-L. This suggests lower liquefaction resistance in the PA-AC-L sample.

In Fig. 8, the cyclic liquefaction resistance curves for all PA samples are summarized, with both stress- and strain-based definitions of initial liquefaction chosen as the first time either r_u reaches 0.99 or the single amplitude of shear strain γ_{SA} exceeds 3%, respectively. Both definitions provide similar observations. It is observed

© ASCE   04024028-6   J. Geotech. Geoenviron. Eng.

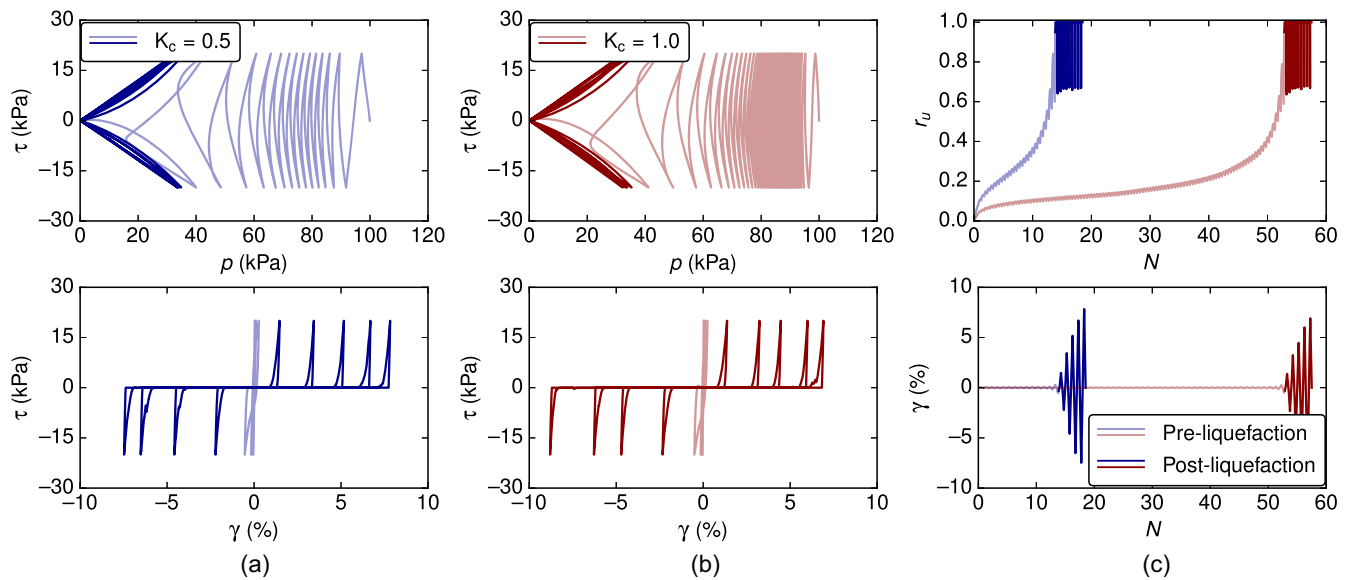J. Geotech. Geoenviron. Eng., 2024, 150(5): 04024028

Fig. 6. Macroscopic response of constant-volume cyclic simple shear simulations for PA medium-dense samples under CSR = 0.20: (a) data for $K_c = 0.5$ (PA-AC-M); (b) data for $K_c = 1.0$ (PA-IC-M); and (c) comparing the samples for evolutions of excess pore pressure ratio and shear strain.
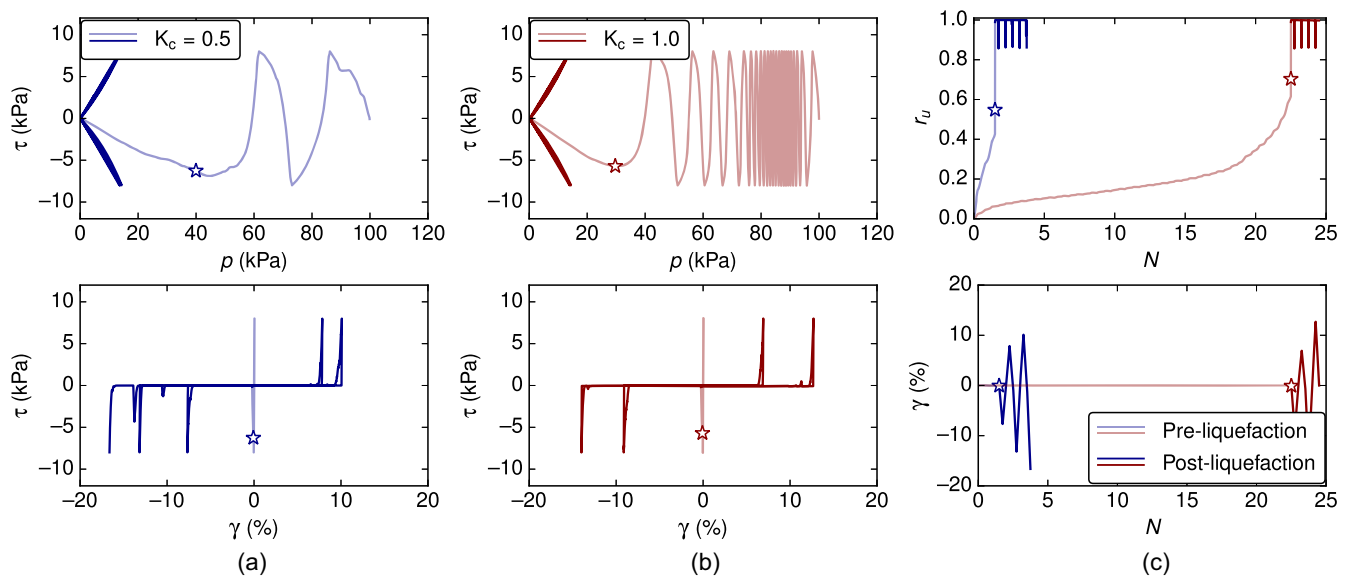

Fig. 7. Macroscopic response of constant-volume cyclic simple shear simulations for PA loose samples under CSR = 0.08: (a) data for $K_c = 0.5$ (PA-AC-L); (b) data for $K_c = 1.0$ (PA-IC-L); and (c) comparing the samples for evolutions of excess pore pressure ratio and shear strain.

that the cyclic liquefaction resistance of PA-M and PA-L samples apparently increases with increasing K_c, or IC samples present higher liquefaction resistance than AC ones, which is consistent with the findings of Georgiannou and Konstadinou (2014), although a different cyclic loading pattern was adopted. The K_c effect on the cyclic liquefaction resistance of PA-D samples is negligible, seemingly consistent with the findings of Ishihara et al. (1977) and Tatsuoka et al. (1982) for samples with $D_r \simeq 50\%$. However, this comparison is not fair since the cyclic resistance ratio $CRR_{20} \simeq 0.5$ (CSR causing initial liquefaction in 20 cycles) is much larger than their $CRR_{20} (\simeq 0.2)$, although these samples share similar D_r. This means that the PA-D samples have much stronger internal structure

or behave like samples with higher D_r (say $\simeq 75\%$) than theirs. If one follows the latter statement, the observation about PA-D samples is different from Tatsuoka et al. (1982), who noticed higher liquefaction resistance for samples with $D_r > 70\%$. Additionally, PA samples with higher $D_r \simeq 69\%$ (not presented in this paper) were also tested, and both IC and AC samples provide $CRR70 \simeq 1.2$ (CSR causing initial liquefaction in 70 cycles), which means that further increasing D_r does not see the reverse trend of K_c effect as postulated by Georgiannou and Konstadinou (2014). In summary, the effect of K_c on the cyclic liquefaction resistance of PA samples was found to depend on D_r. For loose and medium-dense samples, IC samples exhibited higher liquefaction resistance than
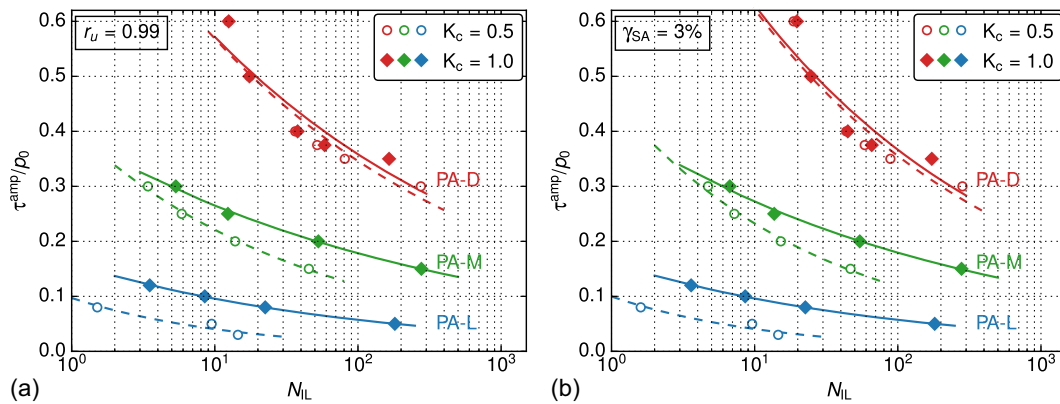
© ASCE 04024028-7 J. Geotech. Geoenviron. Eng.

J. Geotech. Geoenviron. Eng., 2024, 150(5): 04024028

Fig. 8. Cyclic liquefaction resistance curves for PA samples with varying levels of D_r and K_c, using two different approaches to define initial liquefaction: (a) $r_u = 0.99$; and (b) $\gamma_{SA} = 3\%$.

AC samples. However, with increasing D_r, the difference in cyclic liquefaction resistance between the two types of samples decreased until it became negligible.

Results from PB Samples

The stress path and stress-strain response of the PB samples are qualitatively similar to those of the PA samples. However, the PB-D and PB-M samples exhibit a faster transition to initial liquefaction compared to the PA-D and PA-M samples, respectively, which can be attributed to the distinct sample preparation protocols leading to variations in the inherent fabric of the samples. In the interest of brevity, the stress path and stress-strain response for the PB samples are not presented here. Instead, Fig. 9 displays the cyclic liquefaction resistance curves for all the PB samples, which reveals two remarkable findings. The effect of K_c on the liquefaction resistance of PB samples becomes insignificant, regardless of D_r. Additionally, compared to the corresponding PA samples shown in Fig. 8, the dense and medium-dense PB samples exhibit substantially lower cyclic liquefaction resistance curves. For instance, the CRR_{20} for PB-D samples is approximately 0.3, which is closer to the CRR_{20} of laboratory samples with similar D_r found in the literature (e.g., Ishihara et al. 1977; Tatsuoka et al. 1982; Vargas et al. 2020).

Although the CRR_{20} of PB-M samples (0.11) falls between those of PA-IC-M (0.24) and PA-IC-L (0.08), treating PB-M samples as PA samples with D_r ranging between 10% and 30% creates a contradiction. This is because PA-IC samples in that range of D_r exhibit much higher liquefaction resistance than PA-AC samples, which is not the case for PB-M samples. Therefore, PB-M samples are genetically different from PA-M or PA-L samples, and this issue will be explored in more detail later.

Results from PC Samples

Six PC samples were constructed, consisting of three dense, two medium-dense, and one loose sample. Comparing the PC-D1 samples with the PA-D and PB-D samples, there were no qualitatively distinct responses, except for the reduced number of loading cycles approaching initial liquefaction. This observation also applied to the PC-D2 and PC-D3 samples. In other words, all PC-D samples listed in Table 2 exhibited cyclic mobility-type liquefaction. The stress path and stress-strain response of the PC samples were not presented for the same reasons as the PB samples. While the three PC-D samples presented in Table 2 exhibited cyclic mobility-type liquefaction, it is worth noting that by reducing μ_I to the extreme of
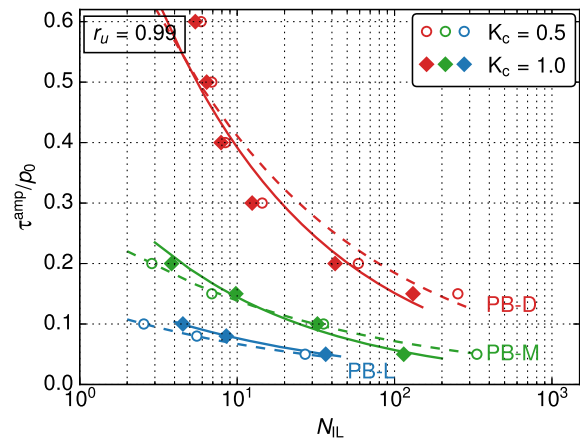

Fig. 9. Cyclic liquefaction resistance curves ($r_u = 0.99$) for PB samples with varying levels of D_r and K_c.

0.5, one can prepare a PC-D sample that exhibits flow liquefaction. This indicates the importance of inherent fabric induced by sample preparation protocols in addition to D_r.

As flow liquefaction is not expected at $D_r > 50\%$ in typical laboratory sample preparation techniques for sands, the corresponding PC samples that experience flow liquefaction are not presented in Table 2. It is worth noting that laboratory tests on sands have shown the occurrence of flow liquefaction for such densities in some consecutive re-liquefaction scenarios (e.g., Yamada et al. 2010; Amini et al. 2021; Yang et al. 2022b). This suggests that flow liquefaction at such densities is possible under certain fabric conditions for sands. PC-M2 is a medium-dense PC sample that presents flow liquefaction in the cyclic simple shear simulations (stress–strain response not shown). This sample is maintained in the database with the purpose of checking whether liquefaction type (cyclic mobility versus flow liquefaction) influences the K_c effect on the cyclic liquefaction resistance.

The cyclic liquefaction resistance curves for all PC samples are summarized in Fig. 10. Fig. 10(a) reveals a variety of K_c effects on the cyclic liquefaction resistance of PC-D samples at similar D_r. The PC-AC-D1 sample presents higher liquefaction resistance than PC-IC-D1, with CRR_{20} of 0.33 versus 0.20, respectively, consistent with the findings of Hosono and Yoshimine (2008) and Vargas et al. (2020). This trend, however, is reversed for PC-D2 samples,
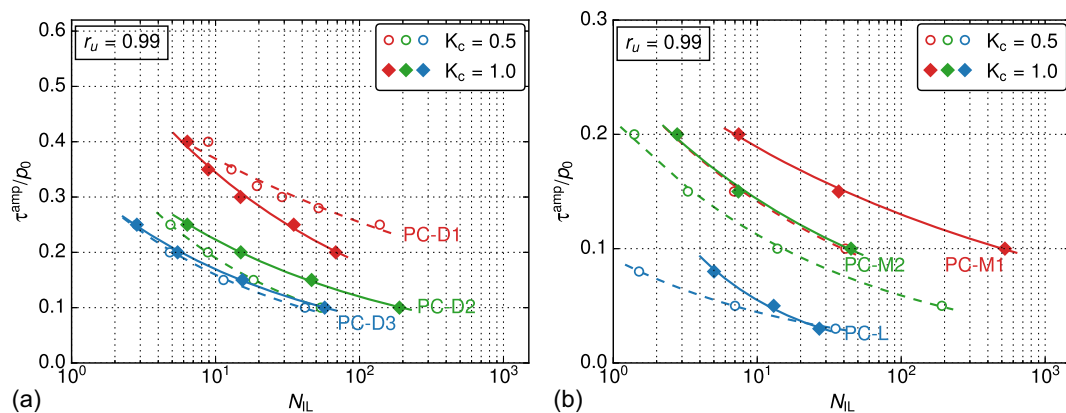
© ASCE 04024028-8 J. Geotech. Geoenviron. Eng.

J. Geotech. Geoenviron. Eng., 2024, 150(5): 04024028

Fig. 10. Cyclic liquefaction resistance curves ($r_u = 0.99$) for PC samples with varying levels of D_r and K_c.

with CRR$_{20}$ of 0.18 versus 0.15, respectively, which agrees with Georgiannou and Konstadinou (2014). The K_c effect on the cyclic liquefaction resistance of PC-D3 samples appears to be negligible, similar to the cases of PA-D, PB-D, and PB-M samples, consistent with the early finding of Ishihara et al. (1977).

It is worth noting that the PC samples were prepared using the same sample preparation protocol, with the only difference being the μ_I value, which was used to mimic a lubrication effect during the sample preparation process. Surprisingly, the resulting PC samples exhibited different K_c effects on the cyclic liquefaction resistance for the dense samples. While it is acknowledged that the idealized PC protocol may not precisely replicate the actual sample preparation procedures utilized in the referenced experimental studies, it can be inferred from our current observations that the controversial results obtained in prior laboratory experiments may be attributed to variations in sample preparation protocols. The K_c effect on the cyclic liquefaction resistance of PC-M1 and PC-M2 samples, as shown in Fig. 10(b), was consistent with the effect observed in PA-M and PA-L samples. Specifically, the IC samples exhibited higher liquefaction resistance compared to the AC samples, which was only reported by Georgiannou and Konstadinou (2014).

Summary

The cyclic resistance ratio CRR$_{20}$ values, which represent the cyclic liquefaction resistance induced by the cyclic stress ratio (CSR) after twenty loading cycles, were extracted from the cyclic liquefaction resistance curves shown in Figs. 8–10. The relationship between CRR$_{20}$ and D_r is illustrated in Fig. 11. For $D_r \gtrsim 30\%$, the PA samples exhibited significantly higher CRR$_{20}$ values compared to the PB and PC samples. This difference becomes more pronounced as D_r increases. Among the PC samples, it was observed that higher relative densities did not necessarily result in higher cyclic liquefaction resistance.

Fig. 11 emphasizes the complexities of the K_c effect on the cyclic liquefaction resistance of granular materials. It indicates a clear dependence on relative density and sample preparation protocol. Unlike D_r, the specific effects of different sample preparation protocols on the cyclic liquefaction resistance have not yet been thoroughly assessed, and there is a lack of indicators that can effectively differentiate between various protocols. However, the striking similarity between Figs. 11 and 3(a) provides a promising indication that can serve as a valuable guide for deriving a universal explanation of the K_c effect on the cyclic liquefaction resistance of granular materials. This significant correlation motivates further
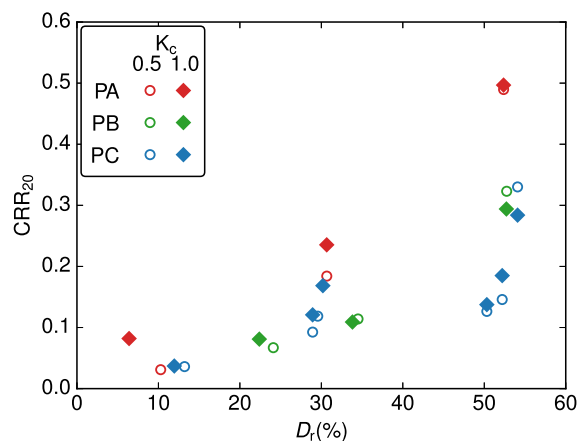

Fig. 11. Relation between cyclic resistance ratio (CRR$_{20}$), resulting in initial liquefaction ($r_u = 0.99$) after twenty cycles, and relative density (D_r) for all DEM samples.

investigation in the subsequent sections to unravel a comprehensive understanding of the underlying mechanisms.

Initial State and K_c-Enhanced Liquefaction Resistance

Several macroscopic and microscale descriptors, such as initial shear wave velocity, initial state parameter, and initial values of coordination number and fabric anisotropy, have exhibited strong correlations with cyclic liquefaction resistance. This section employs these descriptors with the aim of establishing a more universal correlation by incorporating the K_c effect. The effect of anisotropic consolidation on liquefaction resistance is primarily presumed to be associated with the inherent properties of the samples, specifically focusing on the examination of the packing properties of the samples at the onset of the constant-volume cyclic shearing stage. Further analysis considering the evolution of contact network may be valuable but not within the scope of this study.

Initial Shear Wave Velocity

The initial shear wave velocity V_{s0} has been widely used to correlate with cyclic liquefaction resistance of isotropically consolidated
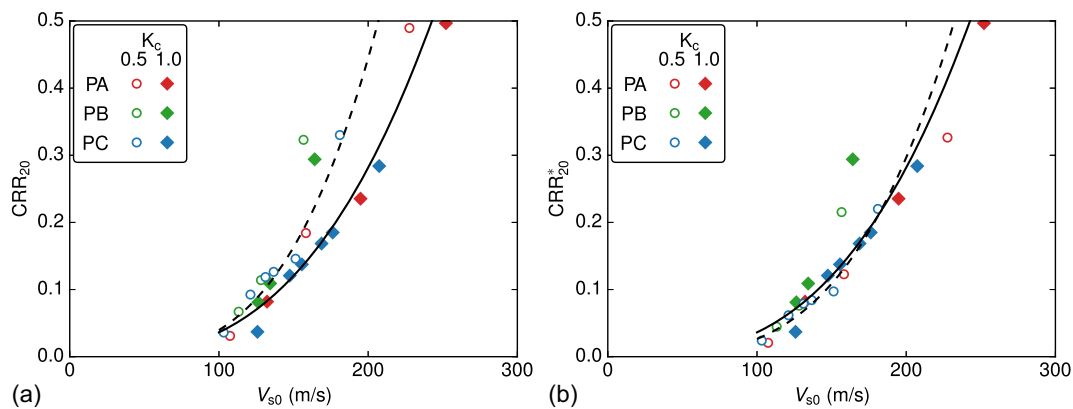
© ASCE   04024028-9   J. Geotech. Geoenviron. Eng.

J. Geotech. Geoenviron. Eng., 2024, 150(5): 04024028

Fig. 12. Correlation between cyclic liquefaction resistance ratios and initial shear wave velocity V_{s0}: (a) CRR_{20}; and (b) CRR^*_{20}. The dashed and solid lines represent the power function trends for $K_c = 0.5$ and 1.0, respectively.

soil samples under undrained cyclic triaxial loading (e.g., Tokimatsu et al. 1986; Tokimatsu and Uchida 1990; Chen et al. 2005; Wang et al. 2006; Zhou and Chen 2007; Baxter et al. 2008; Ahmadi and Paydar 2014). Laboratory data from these studies indicate that at constant effective confining stress, the correlation between cyclic resistance ratio CRR and V_{s0} for a given soil is independent of the sample preparation methods and stress history but dependent on the soil type, i.e., the correlation is not unique for all soils. From the DEM simulations of undrained cyclic triaxial tests on samples with various relative densities, confining pressures, and microparameters, Xu et al. (2015) further identified two microparameters including interparticle friction and particle shear modulus that noticeably affect the uniqueness of the CRR-V_{s0} relationship.

In this paper, the initial shear modulus G_0 is approximated by the average small-strain shear modulus with $\gamma < 2 \times 10^{-5}$, based on linearizing the stress-strain curve τ-γ of constant-p simple shear simulations (as introduced later) in the very beginning of shearing, whose values are reported in Table 2. V_{s0} is thus obtained by

$$V_{s0} = \sqrt{\frac{G_0}{\rho_{sat}}} \quad (8)$$

with the saturated density $\rho_{sat} = (\rho + \rho_w e_0)/(1 + e_0)$ and ρ_w denoting water density. It should be noted that we do not explicitly model water in the simulation and adding ρ_w in Eq. (8) does not change the following observations noticeably. Another method to measure shear wave velocity in the DEM model, mentioned by Xu et al. (2015), is simulation of the propagation of a velocity pulse. They compared V_{s0} values from both methods and did not reveal noticeable difference when the sample had very small deformation.

Fig. 12(a) presents the relationship between CRR_{20} and V_{s0} for all the DEM samples listed in Table 2. The scattered data points in Fig. 11 become more condensed and well-organized in Fig. 12, suggesting the advantage of utilizing V_{s0} over D_r in correlating with cyclic liquefaction resistance. Although a clear collapsing CRR_{20} and V_{s0} relationship is not observed for all the samples, AC samples tend to exhibit higher CRR_{20} values at similar V_{s0}. The data points for IC or AC samples, except PB-D samples, indicate a power relationship in the form

$$CRR_{20} \propto (V_s)^\beta \quad (9)$$

with $\beta \simeq 3.49$ for $K_c = 0.5$ and $\beta \simeq 2.96$ for $K_c = 1.0$, suggesting the influence of K_c on the CRR_{20} and V_{s0} relation. However, if we define CSR with respect to the initial vertical normal stress σ_{v0}, the associated cyclic stress ratio CRR^*_{20} is linked to CRR_{20} as follows:

$$CRR^*_{20} = \left(\frac{\tau^{amp}}{\sigma_{v0}}\right)_{20} = \left(\frac{1 + 2K_c}{3}\frac{\tau^{amp}}{p_0}\right)_{20} = \frac{1 + 2K_c}{3}CRR_{20} \quad (10)$$

which helps decrease the CRR value. Thus a similar correlation function to Eq. (9) is introduced as

$$CRR^*_{20} \propto (V_s)^\beta \quad (11)$$

Fig. 12(b) displays the relationship between CRR^*_{20} and V_{s0}, where all the data points, excluding PB-D samples, appear to follow a similar power function, indicating the negligible effect of K_c on the CRR^*_{20} and V_{s0} relation. This observation provides a compelling rationale for advocating the definition of CSR in simple shear tests with respect to σ_{v0} rather than p_0. Therefore, the approximately unique relationship between CRR^*_{20} and V_{s0} offers an approach to assess the effect of K_c on cyclic liquefaction resistance. Given the V_{s0} values for two samples with different K_c, one can approximate CRR^*_{20} using the $CRR^*_{20} - V_{s0}$ relationship. Eq. (10) allows us to determine the CRR_{20} value for each sample.

State Parameter

In addition to the initial shear wave velocity, the initial state parameter ψ_{e0} has also been widely used to correlate with the cyclic liquefaction resistance of soils in laboratory experimental data (e.g., Yang and Sze 2011; Porcino et al. 2021) and DEM studies (e.g., Gu et al. 2020; Rahman et al. 2021; Banerjee et al. 2023, 2024). The state parameter ψ_e, introduced by Been and Jefferies (1985), quantifies the difference between the current void ratio e and the critical state void ratio e_c at the same mean stress p, represented as $\psi_e = e - e_c$. Here, ψ_{e0} denotes the state parameter at the beginning of cyclic shearing. Recent studies have revealed that the cyclic liquefaction resistance generally decreases with increasing initial state parameter ψ_{e0}, although a unique relationship between CRR and ψ_{e0} cannot be expected for different soils or even the same soil because the initial fabric effects are not accounted for in ψ_{e0} (Jefferies and Been 2015). Similarly, Gu et al. (2020) suggested a state parameter ψ_z with respect to coordination number, denoted as $\psi_z = z_m - z_{mc}$, where ψ_{z0} considered the initial fabric effect to some extent and exhibited a better linkage with cyclic liquefaction resistance.

In this study, the approach proposed by Banerjee et al. (2023) was adopted to determine ψ_{e0} and ψ_{z0} for each sample. A special strain control constant-p shearing protocol was employed to directly deduce the values of e_c and z_{mc} corresponding to p_0. In this protocol, biperiodic boundary conditions were applied to the lateral sides of the sample box, and the normal stresses, including σ_{xx}, σ_{yy},

© ASCE   04024028-10   J. Geotech. Geoenviron. Eng.

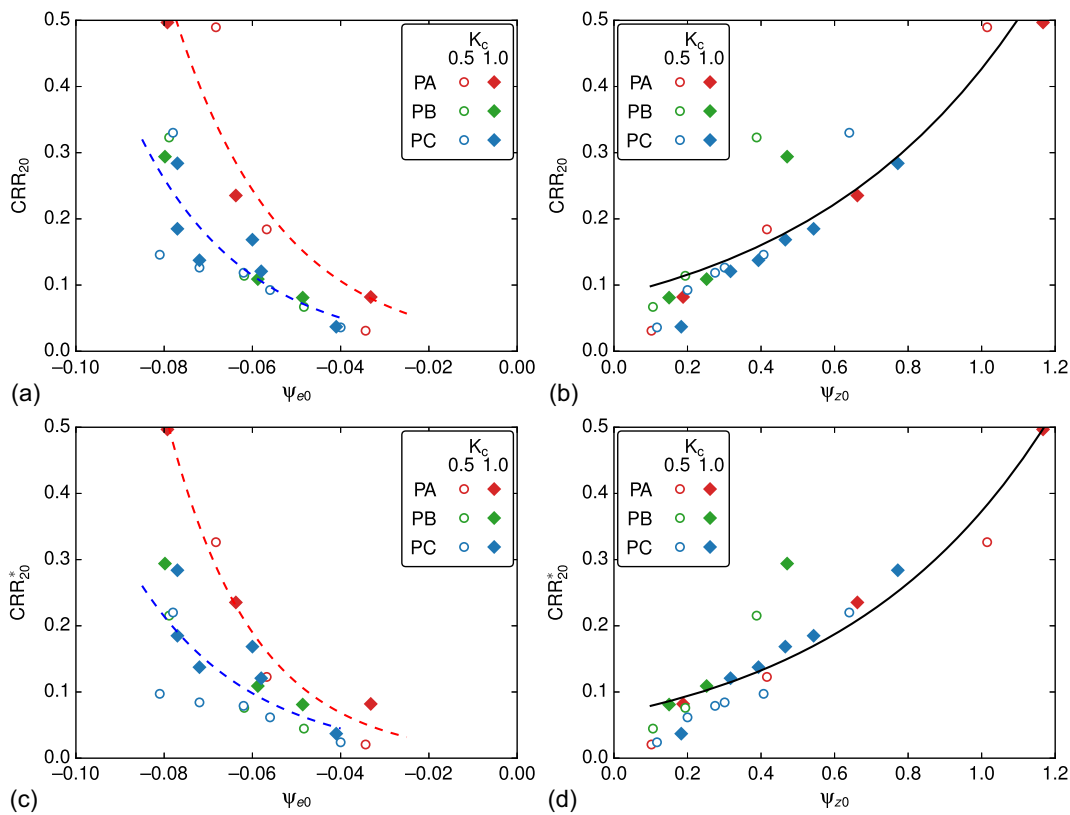J. Geotech. Geoenviron. Eng., 2024, 150(5): 04024028

Fig. 13. Correlations of cyclic resistance ratios CRR_{20} or CRR_{20}^* and initial macro and micro state parameters: (a and c) for void ratio-based state parameter ψ_{e0}; and (b and d) for coordination number-based state parameter ψ_{z0}.

and σ_{zz}, were maintained constant using a servo-control algorithm. The sample was sheared under a constant shear velocity applied to the top wall along the x direction. As a result, variations in shear stress occurred until the sample reached a state close to the critical state, where shear stress τ and void ratio e reached a nearly steady state. The corresponding values of e_c and z_{mc} at this state are also listed in Table 2. It is worth noting that the variations in e_c and z_{mc} were not significant, given the uniqueness of the critical state condition for samples with the same particle properties.

Fig. 13 presents the relationship between CRR_{20} or CRR_{20}^* and the state parameters ψ_{e0} and ψ_{z0}. The data points are fitted with an exponential function given by

$$CRR_{20}\,(\text{or}\,CRR_{20}^*) \propto e^{-n\psi_{e0}}; \qquad CRR_{20}\,(\text{or}\,CRR_{20}^*) \propto e^{k\psi_{z0}} \quad (12)$$

where n and k are positive fitting parameters. In Fig. 13(a), the data points for PA are clearly positioned above those for PB and PC, highlighting the limitations of linking CRR_{20} with ψ_{e0} as mentioned by Jefferies and Been (2015). This limitation persists when substituting CRR_{20} with CRR_{20}^*, as shown in Fig. 13(c). The advantage of ψ_{z0} over ψ_{e0} when linking with cyclic liquefaction resistance is revealed by the convergence of data points in Figs. 13(b and d), indicating a consistent relationship irrespective of K_c value, despite outliers from PB-D samples. It can be approximated that CRR_{20} or CRR_{20}^* increases with increasing ψ_{z0}, and the diverse effects of K_c on CRR_{20} can be attributed to the differences in ψ_{z0} or even z_{m0}, considering the slight variations in z_{mc} among different samples. Based on this, it can be postulated that the K_c effect on cyclic liquefaction resistance, depending on the sample preparation protocol, is actually governed by the initial coordination number

z_{m0}, which may serve as the microscopic origin for the initial shear wave velocity V_{s0}.

Coordination Number and Fabric Anisotropy

The more highly scattered pattern between CRR_{20}^* and ψ_{z0} (or z_{m0}) in Fig. 13(d) compared with the relation of CRR_{20}^* and V_{s0} in Fig. 12(b) indicates something missing in the micromechanical analysis. Here a higher order microscopic descriptor, i.e., the contact normal-based fabric anisotropy a_{c0} is introduced and combined with z_{m0} to be linked with the cyclic liquefaction resistance of granular materials. Recently Otsubo et al. (2022) investigated samples with the same z_{m0} but varying a_{c0} to isolate the influence of a_{c0} and found that the cyclic liquefaction resistance under constant-volume cyclic triaxial loading decreases as a_{c0} increases. This finding, combined with the study by Gu et al. (2020) indicating that liquefaction resistance increases with higher z_{m0}, suggests that for the same material, liquefaction resistance tends to increase with higher coordination number or lower contact normal-based fabric anisotropy. This hypothesis is derived from two independent studies that utilized undrained cyclic triaxial simulations of spherical particles. However, further investigation is required to determine whether the hypothesis can be extended to different loading conditions, such as simple shear, and to ascertain the potential impact of other particle properties, such as particle shape. Nonetheless, a simple exponential function was adopted to establish the relation between CRR_{20}^* and (z_{m0}, a_{c0}), as

$$CRR_{20}^* \propto e^{kz_{m0}-ma_{c0}} \quad (13)$$

with k and m = positive fitting parameters.

© ASCE   04024028-11   J. Geotech. Geoenviron. Eng.

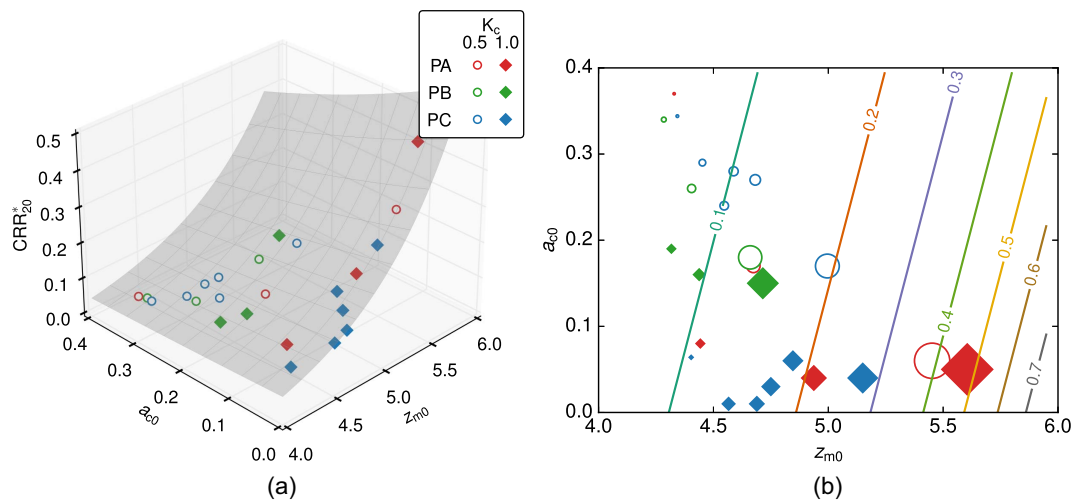J. Geotech. Geoenviron. Eng., 2024, 150(5): 04024028

Fig. 14. Relationship between (a) cyclic resistance ratio CRR_{20}^* and initial values of coordination number and fabric anisotropy (z_{m0}, a_{c0}); and (b) a_{c0} and z_{m0}, with marker size indicating the magnitude of CRR_{20}^* and contours obtained from the fitting function of (a).
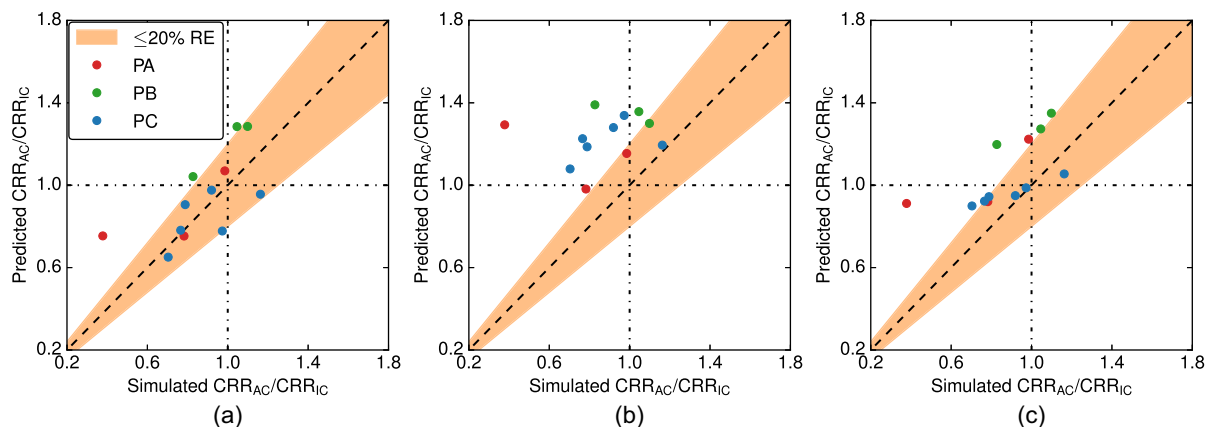

Fig. 15. Comparison of CRR_{AC}/CRR_{IC} between DEM simulations and predictions using correlation functions based on CRR_{20}^* and (a) initial shear wave velocity; (b) initial state parameter associated with mechanical coordination number; and (c) inherent fabric.

To verify this hypothesis, the DEM simulation data was used to determine the fitting parameters k and m. This process did not involve the imposition of constraints that ensure positive fitting parameters. Fig. 14(a) presents the relationship between CRR_{20}^* and (z_{m0}, a_{c0}) based on the simulation data. The fitting surface followed Eq. (13) with $k \simeq 1.252$ and $m \simeq 1.226$, in good agreement with the hypothesis, confirming the general trend that CRR_{20}^* increases with increasing z_{m0} or decreasing a_{c0}. Additionally, Fig. 14(b) shows the contour of the fitting function in the $a_{c0} - z_{m0}$ plane, where the marker size of data points represents the magnitude of CRR_{20}^*. The noticeable inclination of the contours, whose slope angle is quantified by the ratio $k/m (\simeq 1.02)$, graphically demonstrates the coupling effect of z_{m0} and a_{c0} on the CRR_{20}^* value. The assumed linear relationship between a_{c0} and z_{m0} in influencing CRR_{20}^* implies the similar amount of contribution for the same amount of increment in z_{m0} or decrement in a_{c0}, which should be revisited with a larger dataset.

Performance in Capturing K_c Effect

The earlier parts of this section established three correlation functions linking liquefaction resistance CRR_{20}^* with three different initial descriptors as shown in Eqs. (11)–(13), with their performance illustrated in Figs. 12–14, respectively. To assess their utility in inferring the effect of K_c on CRR_{20}, one can determine the CRR_{20}^* value of the sample based on the relevant initial descriptors and then convert it to CRR_{20} using Eq. (10). For samples with distinct K_c values, the influence of K_c on the liquefaction resistance can be quantified by comparing the ratios of CRR_{AC} and CRR_{IC}. The ratio obtained through correlation functions is denoted as predicted CRR_{AC}/CRR_{IC}. Fig. 15 presents the comparisons between predicted CRR_{AC}/CRR_{IC} and simulated CRR_{AC}/CRR_{IC}, where the latter are directly obtained from DEM simulations. To evaluate the performance of each correlation function, two metrics are introduced: (1) the percentage of data points within 20% relative error ($\leq$20% RE) indicated by the shaded area, and (2) the qualitative trend indicating whether the data points fall into the first and third quadrants. By counting the number of successful cases that satisfy each metric, it can be concluded that the correlation function associated with initial shear wave velocity exhibits the best performance, followed by the inherent fabric and the initial state parameter. These two metrics serve as measures of the goodness of fit, similar to R-squared. It is important to note that this study provides a limited database, making cross-validation, as commonly employed

in machine learning models, unfeasible at this stage. However, it remains a possibility in the future as more data is accumulated.

Conclusions

This study investigated the effect of anisotropic consolidation, K_c, on the cyclic liquefaction resistance of granular materials through 3D-DEM constant-volume cyclic simple shear simulations. Two types of DEM samples, anisotropically consolidated (AC) with $K_c = 0.5$ and isotropically consolidated (IC) with $K_c = 1$, were constructed at the similar confining stress p_0 and relative density D_r following three sample preparation protocols (PA, PB, and PC). Three levels of D_r were considered, denoted as dense (D), medium dense (M), and loose (L). These samples were then subjected to constant-volume cyclic simple shearing to determine the liquefaction resistance, which was quantified by the cyclic resistance ratio CRR_{20}.

This study revealed that the effect of K_c on the cyclic liquefaction resistance of granular materials could be influenced by the sample preparation method in different ways. The results indicated that PA-IC specimens exhibited higher cyclic liquefaction resistance compared to PA-AC specimens, and the difference reduced as the relative density D_r increased. However, PB-IC and AC samples exhibited similar cyclic liquefaction resistance, irrespective of D_r. In the case of PC-M and PC-L samples, the IC specimens showed higher liquefaction resistance than their AC counterparts. The K_c effect on the cyclic liquefaction resistance of PC-D specimens was found to be highly dependent on the tangential friction coefficient μ_I used in the sample preparation.

The observed discrepancies in liquefaction resistance were attributed to the initial properties of the samples prior to constant-volume cyclic simple shearing. Three types of initial descriptors, including the macroscale initial shear wave velocity (V_{s0}), and the microscopic level initial state parameter associated with coordination number (ψ_{z0}) and inherent fabric quantified by (z_{m0}, a_{c0}), showed strong correlations with CRR_{20}^*, regardless of K_c values. Here CRR_{20}^* is associated with the CSR defined by τ^{amp}/σ_{v0}, behaving as the CRR_{20} with K_c embedded. These correlation functions offer a means to infer the effect of K_c on CRR_{20}. Based on the database established in this study, the $CRR_{20}^* - V_{s0}$ relation demonstrates the best performance in capturing the K_c effect, followed by the $CRR_{20}^* - (z_{m0}, a_{c0})$ and $CRR_{20}^* - \psi_{z0}$ relations. While the macroscale V_{s0} is widely utilized in practical applications, the microscopic parameters shine a light on the inner workings of V_{s0}. The findings presented here underscore a potential connection between shear wave velocity and fabric, as also observed in recent studies (e.g., Mital et al. 2020; Li et al. 2023; Gu et al. 2023), but now in the context of cyclic liquefaction. This insight, particularly in understanding and unifying the influence of K_c on cyclic liquefaction resistance, is of significant importance.

Overall, the results of this study enhance the understanding of the influence of anisotropic consolidation on the cyclic liquefaction resistance of granular materials. The findings emphasize the significance of sample preparation protocols and inherent fabric characteristics in determining the liquefaction resistance. The correlations established between initial properties and liquefaction resistance provide valuable insights for evaluating and predicting the liquefaction potential of granular materials in geotechnical engineering applications. Future research endeavors should explore additional descriptors and further refine the understanding of inherent anisotropy to enhance the accuracy of liquefaction resistance predictions.

Data Availability Statement

Some or all data, models, or code that support the findings of this study are available from the corresponding author upon reasonable request.

References

Agnolin, I., and J.-N. Roux. 2007. "Internal states of model isotropic granular packings. I. Assembling process, geometry, and contact networks." *Phys. Rev. E* 76 (6): 061302. https://doi.org/10.1103/PhysRevE.76.061302.

Ahmadi, M. M., and N. A. Paydar. 2014. "Requirements for soil-specific correlation between shear wave velocity and liquefaction resistance of sands." *Soil Dyn. Earthquake Eng.* 57 (Mar): 152–163. https://doi.org/10.1016/j.soildyn.2013.11.001.

Ai, J., J.-F. Chen, J. M. Rotter, and J. Y. Ooi. 2011. "Assessment of rolling resistance models in discrete element simulations." *Powder Technol.* 206 (3): 269–282. https://doi.org/10.1016/j.powtec.2010.09.030.

Amini, P. F., D. Huang, G. Wang, and F. Jin. 2021. "Effects of strain history and induced anisotropy on reliquefaction resistance of Toyoura sand." *J. Geotech. Geoenviron. Eng.* 147 (9): 04021094. https://doi.org/10.1061/(ASCE)GT.1943-5606.0002588.

Banerjee, S. K., M. Yang, and M. Taiebat. 2023. "Effect of coefficient of uniformity on cyclic liquefaction resistance of granular materials." *Comput. Geotech.* 155 (Mar): 105232. https://doi.org/10.1016/j.compgeo.2022.105232.

Banerjee, S. K., M. Yang, and M. Taiebat. 2024. "Effect of particle shape on cyclic liquefaction resistance of granular materials." *Acta Geotech.* 32 (Jan): 1–16. https://doi.org/10.1016/j.compgeo.2022.105232.

Baxter, C. D. P., A. S. Bradshaw, R. A. Green, and J.-H. Wang. 2008. "Correlation between cyclic resistance and shear-wave velocity for providence silts." *J. Geotech. Geoenviron. Eng.* 134 (1): 37–46. https://doi.org/10.1061/(ASCE)1090-0241(2008)134:1(37).

Been, K., and M. G. Jefferies. 1985. "A state parameter for sands." *Géotechnique* 35 (2): 99–112. https://doi.org/10.1680/geot.1985.35.2.99.

Boulanger, R. W., and R. B. Seed. 1995. "Liquefaction of sand under bidirectional monotonic and cyclic loading." *J. Geotech. Eng.* 121 (12): 870–878. https://doi.org/10.1061/(ASCE)0733-9410(1995)121:12(870).

Chen, Y., H. Ke, and R.-P. Chen. 2005. "Correlation of shear wave velocity with liquefaction resistance based on laboratory tests." *Soil Dyn. Earthquake Eng.* 25 (6): 461–469. https://doi.org/10.1016/j.soildyn.2005.03.003.

Georgiannou, V. N., and M. Konstadinou. 2014. "Effects of density on cyclic behaviour of anisotropically consolidated Ottawa sand under undrained torsional loading." *Géotechnique* 64 (4): 287–302. https://doi.org/10.1680/geot.13.P.090.

Ghoraiby, M. E., H. Park, and M. T. Manzari. 2020. "Physical and mechanical properties of Ottawa F65 sand." In *Model tests and numerical simulations of liquefaction and lateral spreading*, 45–67. Cham, Switzerland: Springer.

Gu, X., X. Liang, and J. Hu. 2023. "Quantifying fabric anisotropy of granular materials using wave velocity anisotropy: A numerical investigation." *Géotechnique* 1–13. https://doi.org/10.1680/jgeot.22.00314.

Gu, X., J. Zhang, and X. Huang. 2020. "DEM analysis of monotonic and cyclic behaviors of sand based on critical state soil mechanics framework." *Comput. Geotech.* 128 (Mar): 103787. https://doi.org/10.1016/j.compgeo.2020.103787.

Guo, N., and J. Zhao. 2013. "The signature of shear-induced anisotropy in granular media." *Comput. Geotech.* 47 (Jan): 1–15. https://doi.org/10.1016/j.compgeo.2012.07.002.

© ASCE

04024028-13

J. Geotech. Geoenviron. Eng.

Hosono, Y., and M. Yoshimine. 2008. "Effects of anisotropic consolidation and initial shear load on liquefaction resistance of sand in simple shear condition." In Vol. 4 of *Proc., Geotechnical Engineering for Disaster Mitigation and Rehabilitation*, 352–358. Berlin: Springer.

Huang, X., C.-Y. Kwok, K. J. Hanley, and Z. Zhang. 2018. "DEM analysis of the onset of flow deformation of sands: Linking monotonic and cyclic undrained behaviours." *Acta Geotech.* 13 (5): 1061–1074. https://doi.org/10.1007/s11440-018-0664-3.

Ishihara, K., S. Iwamoto, S. Yasuda, and H. Takatsu. 1977. "Liquefaction of anisotropically consolidated sand." In Vol. 2 of *Proc., 9th Int. Conf. on Soil Mechanics and Foundation Engineering, JSSMFE*, 261–264. London: International Society for Soil Mechanics and Geotechnical Engineering.

Ishihara, K., and H. Takatsu. 1979. "Effects of overconsolidation and k0 conditions on the liquefaction characteristics of sands." *Soils Found.* 19 (4): 59–68. https://doi.org/10.3208/sandf1972.19.4_59.

Jefferies, M., and K. Been. 2015. *Soil liquefaction: A critical state approach*. Boca Raton, FL: CRC Press.

Kanatani, K.-I. 1984. "Distribution of directional data and fabric tensors." *Int. J. Eng. Sci.* 22 (2): 149–164. https://doi.org/10.1016/0020-7225(84)90090-9.

Kloss, C., C. Goniva, A. Hager, S. Amberger, and S. Pirker. 2012. "Models, algorithms and validation for opensource DEM and CFD–DEM." *Prog. Comput. Fluid Dyn.* 12 (2–3): 140–152. https://doi.org/10.1504/PCFD.2012.047457.

Kuhn, M. R. 2017. *Granular geomechanics*. Amsterdam, Netherlands: Elsevier.

Kuhn, M. R., H. E. Renken, A. D. Mixsell, and S. L. Kramer. 2014. "Investigation of cyclic liquefaction with discrete element simulations." *J. Geotech. Geoenviron. Eng.* 140 (12): 04014075. https://doi.org/10.1061/(ASCE)GT.1943-5606.0001181.

Li, Y., M. Otsubo, and R. Kuwano. 2023. "Evaluation of soil fabric using elastic waves during load-unload." *J. Rock Mech. Geotech. Eng.* 15 (10): 2687–2700. https://doi.org/10.1016/j.jrmge.2022.12.004.

MiDi, G. D. R. 2004. "On dense granular flows." *Eur. Phys. J. E* 14 (4): 341–365. https://doi.org/10.1140/epje/i2003-10153-0.

Mital, U., R. Kawamoto, and J. E. Andrade. 2020. "Effect of fabric on shear wave velocity in granular soils." *Acta Geotech.* 15 (5): 1189–1203. https://doi.org/10.1007/s11440-019-00766-1.

Mutabaruka, P., M. Taiebat, R. J.-M. Pellenq, and F. Radjai. 2019. "Effects of size polydispersity on random close-packed configurations of spherical particles." *Phys. Rev. E* 100 (4): 042906. https://doi.org/10.1103/PhysRevE.100.042906.

Oda, M. 1982. "Fabric tensor for discontinuous geological materials." *Soils Found.* 22 (4): 96–108. https://doi.org/10.3208/sandf1972.22.4_96.

O'Sullivan, C. 2011. *Particulate discrete element modelling: A geomechanics perspective*. Boca Raton, FL: CRC Press.

Otsubo, M., S. Chitravel, R. Kuwano, K. J. Hanley, H. Kyokawa, and J. Koseki. 2022. "Linking inherent anisotropy with liquefaction phenomena of granular materials by means of DEM analysis." *Soils Found.* 62 (5): 101202. https://doi.org/10.1016/j.sandf.2022.101202.

Porcino, D. D., T. Triantafyllidis, T. Wichtmann, and G. Tomasello. 2021. "Application of critical state approach to liquefaction resistance of sand–silt mixtures under cyclic simple shear loading." *J. Geotech. Geoenviron. Eng.* 147 (3): 04020177. https://doi.org/10.1061/(ASCE)GT.1943-5606.0002470.

Radja, F., and F. Dubois. 2011. *Discrete-element modeling of granular materials*. New York: Wiley.

Rahman, M. M., H. B. K. Nguyen, A. B. Fourie, and M. R. Kuhn. 2021. "Critical state soil mechanics for cyclic liquefaction and postliquefaction behavior: DEM study." *J. Geotech. Geoenviron. Eng.* 147 (2): 04020166. https://doi.org/10.1061/(ASCE)GT.1943-5606.0002453.

Sitharam, T. G. 2003. "Discrete element modelling of cyclic behaviour of granular materials." *Geotech. Geol. Eng.* 21 (4): 297–329. https://doi.org/10.1023/B:GEGE.0000006036.00597.0b.

Sufian, A., A. R. Russell, and A. J. Whittle. 2017. "Anisotropy of contact networks in granular media and its influence on mobilised internal friction." *Géotechnique* 67 (12): 1067–1080. https://doi.org/10.1680/jgeot.16.P.170.

Tatsuoka, F., M. Muramatsu, and T. Sasaki. 1982. "Cyclic undrained stress-strain behavior of dense sands by torsional simple shear test." *Soils Found.* 22 (2): 55–70. https://doi.org/10.3208/sandf1972.22.2_55.

Thornton, C. 2000. "Numerical simulations of deviatoric shear deformation of granular media." *Géotechnique* 50 (1): 43–53. https://doi.org/10.1680/geot.2000.50.1.43.

Tokimatsu, K., and A. Uchida. 1990. "Correlation between liquefaction resistance and shear wave velocity." *Soils Found.* 30 (2): 33–42. https://doi.org/10.3208/sandf1972.30.2_33.

Tokimatsu, K., T. Yamazaki, and Y. Yoshimi. 1986. "Soil liquefaction evaluations by elastic shear moduli." *Soils Found.* 26 (1): 25–35. https://doi.org/10.3208/sandf1972.26.25.

Vargas, R. R., K. Ueda, and K. Uemura. 2020. "Influence of the relative density and K0 effects in the cyclic response of Ottawa F-65 sand-cyclic Torsional Hollow-Cylinder shear tests for LEAP-ASIA-2019" *Soil Dyn. Earthquake Eng.* 133 (Jun): 106111. https://doi.org/10.1016/j.soildyn.2020.106111.

Wang, G., and J. Wei. 2016. "Microstructure evolution of granular soils in cyclic mobility and post-liquefaction process." *Granular Matter* 18 (3): 51. https://doi.org/10.1007/s10035-016-0621-5.

Wang, J.-H., K. Moran, and C. D. P. Baxter. 2006. "Correlation between cyclic resistance ratios of intact and reconstituted offshore saturated sands and silts with the same shear wave velocity." *J. Geotech. Geoenviron. Eng.* 132 (12): 1574–1580. https://doi.org/10.1061/(ASCE)1090-0241(2006)132:12(1574).

Wei, J., D. Huang, and G. Wang. 2018. "Microscale descriptors for particle-void distribution and jamming transition in pre- and post-liquefaction of granular soils." *J. Eng. Mech.* 144 (8): 04018067. https://doi.org/10.1061/(ASCE)EM.1943-7889.0001482.

Wei, J., and G. Wang. 2017. "Discrete-element method analysis of initial fabric effects on pre-and post-liquefaction behavior of sands." *Géotech. Lett.* 7 (2): 161–166. https://doi.org/10.1680/jgele.16.00147.

Xu, M., Z. Zhang, and X. Huang. 2021. "Identification of jamming transition: A critical appraisal." *Granular Matter* 23 (1): 1–17. https://doi.org/10.1007/s10035-020-01066-2.

Xu, X., D. Ling, Y. Cheng, and Y. Chen. 2015. "Correlation between liquefaction resistance and shear wave velocity of granular soils: A micromechanical perspective." *Géotechnique* 65 (5): 337–348. https://doi.org/10.1680/geot.SIP.15.P.022.

Yamada, S., T. Takamori, and K. Sato. 2010. "Effects on reliquefaction resistance produced by changes in anisotropy during liquefaction." *Soils Found.* 50 (1): 9–25. https://doi.org/10.3208/sandf.50.9.

Yang, J., and H. Y. Sze. 2011. "Cyclic behaviour and resistance of saturated sand under non-symmetrical loading conditions." *Géotechnique* 61 (1): 59–73. https://doi.org/10.1680/geot.9.P.019.

Yang, M., M. Taiebat, P. Mutabaruka, and F. Radjaï. 2021. "Evolution of granular materials under isochoric cyclic simple shearing." *Phys. Rev. E* 103 (Mar): 032904. https://doi.org/10.1103/PhysRevE.103.032904.

Yang, M., M. Taiebat, and F. Radjaï. 2022a. "Liquefaction of granular materials in constant-volume cyclic shearing: Transition between solid-like and fluid-like states." *Comput. Geotech.* 148 (Aug): 104800. https://doi.org/10.1016/j.compgeo.2022.104800.

Yang, S., D. Huang, G. Wang, and F. Jin. 2022b. "Probing fabric evolution and reliquefaction resistance of sands using discrete-element modeling." *J. Eng. Mech.* 148 (6): 04022023. https://doi.org/10.1061/(ASCE)EM.1943-7889.0002104.

Zhang, L., and T. M. Evans. 2020. "Investigation of initial static shear stress effects on liquefaction resistance using discrete element method simulations." *Int. J. Geomech.* 20 (7): 04020087. https://doi.org/10.1061/(ASCE)GM.1943-5622.0001720.

Zhou, Y.-G., and Y.-M. Chen. 2007. "Laboratory investigation on assessing liquefaction resistance of sandy soils by shear wave velocity." *J. Geotech. Geoenviron. Eng.* 133 (8): 959–972. https://doi.org/10.1061/(ASCE)1090-0241(2007)133:8(959).

© ASCE 04024028-14 J. Geotech. Geoenviron. Eng.

J. Geotech. Geoenviron. Eng., 2024, 150(5): 04024028